

See discussions, stats, and author profiles for this publication at: <https://www.researchgate.net/publication/258662067>

# Discrete element modeling of boudinage: Insights on rock rheology, matrix flow, and evolution of geometry

Article in *Journal of Geophysical Research Atmospheres* · January 2012

DOI: 10.1029/2011JB008555

CITATIONS

38

READS

100

2 authors, including:



Janos Urai

RWTH Aachen University and German University of Technology in Oman

441 PUBLICATIONS 7,582 CITATIONS

[SEE PROFILE](#)

Some of the authors of this publication are also working on these related projects:



Grain-scale deformation mechanisms and evolution of porosity in experimentally deformed Boom Clay [View project](#)



Fault dynamics [View project](#)

# Discrete element modeling of boudinage: Insights on rock rheology, matrix flow, and evolution of geometry

Steffen Abe<sup>1</sup> and Janos L. Urai<sup>1,2</sup>

Received 30 May 2011; revised 7 October 2011; accepted 16 October 2011; published 14 January 2012.

[1] We use discrete element model simulations to model the full boudinage process from initial fracturing of intact material to post-fracture flow of material into gaps between fragments and to investigate the role which the material properties of the weak and strong layers play in this process. The models are deformed in 2D plane strain under a range of confining stresses, in coaxial bulk flow. Results show that the material properties, i.e. Mohr-Coulomb or quasi-viscous for the matrix and elastic-brittle for the competent layer, lead to the development of natural looking boudin morphologies and deformation patterns in the matrix. The details of the matrix rheology only have a minor influence on the morphology of the boudins. By varying the material properties of the competent layer between fully brittle and semi-ductile we obtain a wide range of deformation patterns ranging from pinch-and-swell structures to a variety of boudin types including drawn, shear band and straight sided torn boudins. In a number of models we observe rotation of the boudin blocks despite the applied deformation being purely coaxial. These rotations are generally related to asymmetrical (rhombic) boudin shapes. Some features observed in natural boudins such as concave block faces or the formation of veins between fragments are not modeled because pore fluids are not yet included in our model.

**Citation:** Abe, S., and J. L. Urai (2012), Discrete element modeling of boudinage: Insights on rock rheology, matrix flow, and evolution of geometry, *J. Geophys. Res.*, 117, B01407, doi:10.1029/2011JB008555.

## 1. Introduction

[2] Boudins are relatively common structures in layered rocks which have been extended in the direction parallel to the layering [Ramberg, 1955; Ramsay and Huber, 1987; Twiss and Moores, 2007; van Noten and Sintubin, 2010]. However, many aspects of the boudinage process, such as the details of the relation between the rheology of the layers and the fracture spacing or the shape of the boudin blocks are not completely understood yet and therefore remain subject of ongoing research. A wide range of boudin shapes has been observed in nature at the cm- to m-scale [Goscombe *et al.*, 2004]. At the 100 m to km-scale, boudins are common in salt giants [Schönherr *et al.*, 2008; Reuning *et al.*, 2009; van Gent *et al.*, 2011; Kukla *et al.*, 2011]. Those shapes are thought to indicative of the stress and strain conditions and the material properties at the time when the boudins evolved [Goscombe and Passchier, 2003; Maeder *et al.*, 2009]. The separation of the competent layer into boudin blocks during layer-parallel extension can occur through (1) tensile fracture [Ramberg, 1955], (2) shear failure or (3) pinch and swell followed by ductile rupture. In the literature there are two types of approaches to the prediction of size distribution of the fragments.

Fracture saturation models [Bai and Pollard, 1999; Bai *et al.*, 2000; Li and Yang, 2007] predict fracture spacing similar to layer thickness. These models assume elastic deformation in the matrix, elastic-brittle deformation in the competent layer and no-slip interface conditions between the matrix and the competent layer. In contrast, models which incorporate interface slip [Iyer and Podladchikov, 2009] allow for length/width ratios much smaller than 1.0. Recent numerical modeling by Schöpfer *et al.* [2011] shows that full-slip models are a good approximation if the interface coupling is relatively weak but that the 2D stress field inside the competent layer needs to be taken into account in the case of strongly coupled interfaces.

[3] The stress exerted by the matrix on the competent layer, and therefore the fracture spacing and the failure mechanism, depends on the pressure, the deformation rate and the rheology of the matrix and on the degree of coupling between matrix and competent layer. Assuming a strongly simplified model, i.e. constant shear traction along the layer interface and homogeneous stresses across the thickness of the competent layer [Mandl, 2005], the critical length  $L^*$  of the boudin blocks is determined by the tensile strength  $T$  of the competent material and the layer-parallel shear stress  $\sigma_s$  exerted by the matrix and thickness  $d$  of the competent layer:

$$L^* = \frac{Td}{2\sigma_s} \quad (1)$$

[4] In contrast, for purely linear viscous coupling and a homogeneous strain rate in the matrix the shear stress at

<sup>1</sup>Geologie-Endogene Dynamik, RWTH Aachen University, Aachen, Germany.

<sup>2</sup>German University of Technology, Muscat, Oman.

interface between the brittle layer and the matrix can be taken to be linearly dependent on the velocity difference across that interface. Therefore the traction force, and consequently the tensile stress at a given location in the brittle layer, is dependent on the square of the distance from block center [cf. *Ramberg*, 1955, equation 12]. Therefore the critical length is predicted to be proportional to the square root of the strength of the competent layer at a given shear traction:

$$L^* = \alpha\sqrt{Td} \quad (2)$$

where  $\alpha$  is a shear traction parameter which depends on the coupling at the layer-matrix interface and the strain rate in the matrix.

[5] Field observations provide us with the present day geometry of the boudins and allow inferences on the evolution the boudins over time, an on rheology and flow vorticity [*Kenis et al.*, 2005].

[6] Models are an interesting way to investigate the processes involved in the formation of boudin structures. Analogue models [*Ramberg*, 1955; *Neurath and Smith*, 1982; *Ghosh*, 1988; *Kobberger and Zulauf*, 1995; *Kidan and Cosgrove*, 1996; *Harris and Koyi*, 2003; *Victor and Moretti*, 2006; *Zulauf et al.*, 2009, 2010] have provided us with an insight into the evolution of the geometry of boudins in 3D from the initial fracturing to block separation and towards the final 3D structure of the deformed and displaced boudin blocks under well controlled boundary conditions and material rheology. Numerical models have a range of other benefits. The key advantage of numerical models lies in the complete access to all internal variables of the model at all times, giving us access to data which are difficult or impossible to obtain in analogue models, such as the traction forces between the matrix and the competent layer. In addition numerical models are flexible with respect to the boundary applied conditions and, due to the easy repeatability of the simulations, make it easy to perform parameter studies to evaluate the variability of the modeling results. Compared to analogue models they mainly suffer from limited spatial resolution and from limitations to implement the material properties.

[7] Numerical modeling of the full boudinage process presents considerable challenges due to the need to model strongly localized deformation, evolving material discontinuities during the fracture process and very high strains in the flow of the ductile matrix material into the boudin necks. Previous models of boudinage consider either elastic-brittle processes of the fracture initiation phase [*Bai and Pollard*, 1999; *Li and Yang*, 2007; *Iyer and Podladchikov*, 2009; *Schöpfer et al.*, 2011] or the post-fracture deformation phase which is dominated by ductile processes [*Mandal and Khan*, 1991; *Passchier and Druguet*, 2002; *Treagus and Lan*, 2004; *Maeder et al.*, 2009].

[8] Here we present a model of the full evolution of the boudins, including both the brittle failure of the competent layer and the subsequent movement of the boudin blocks in the flow field of the ductile matrix. In this study we restrict the model to 2D in order to enable high resolution at reduced computational cost. This already allows the simulation of many models using a range of different material parameters and boundary conditions. The extension of the models to 3D

does not present significant difficulties and is subject of an ongoing study.

## 2. Method

[9] To model the brittle fracturing of the competent layer we use a discrete element model (DEM) approach [*Cundall and Strack*, 1979; *Mora and Place*, 1994; *Place and Mora*, 1999]. Here the material is represented by a large number of spherical particles interacting with nearest neighbors. Different material properties are achieved by a range of different particle interactions, such as frictional or brittle-elastic. The forces and moments acting on the particles are calculating from these interactions. The movement of the particles is then determined from the particle accelerations due to the forces and moments according to Newton's laws. Time stepping is purely explicit. Therefore a quasi-static approximation is used for static problems, i.e. exact mechanical equilibrium is generally not achieved, unlike, for example, in the "Contact Dynamics" particle model [*Radjai and Richefeu*, 2009].

[10] This approach enables the simulation of a wide range of material behaviors such as brittle-elastic solids or frictional granular materials. Here we also introduce a particle interaction with a velocity dependent dissipative term, resulting in a visco-plastic material behavior (section 3). To enable the simulation of sufficiently large models, the parallel DEM simulation package ESyS-Particle [*Abe et al.*, 2003; *Weatherley et al.*, 2010] (<https://launchpad.net/esys-particle/>) was used.

## 3. Quasi-Viscous Material in DEM

[11] Possible approaches to model viscous behavior in DEM include the coupling of a DEM to a finite element (FEM) model which has been shown to be possible, but difficult [*Abe et al.*, 2005], mainly due to the problems arising from the fact that DEM is Lagrangian whereas FEM is Eulerian.

[12] We extend the existing approach by introducing a new type of particle interactions into an existing DEM software. The new approach does, for the range of velocities and material parameters relevant to this study, provide a good approximation of viscous behavior. In addition, the approach has the advantage of being based strictly on nearest-neighbor particle interactions, therefore fitting very well into the existing DEM framework.

[13] The new interaction type consists of the combination of a purely repulsive linear elastic interaction combined with a "dashpot" type interaction. Given that this type of interaction does not involve tangential forces we are using particles without rotational degrees of freedom and therefore apply the interaction forces to the particle centers instead of the particles surfaces. The force  $f_{ab}^d$  on particle  $a$  due to its dashpot interaction with particle  $b$  is calculated as

$$f_{ab}^d = -Ad_{ab} \frac{\Delta v_{ab}}{r_{ab}} \quad (3)$$

where  $r_{ab}$  is the current distance between the particles,  $d_{ab}$  is a measure of the size or "weight" of the interaction which can be considered in terms of the cross section of the dashpot and is calculated from the average radii of the particles

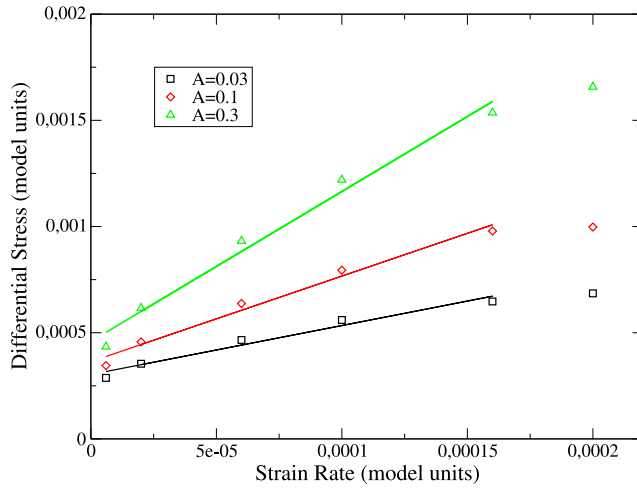


**Figure 1.** Relation between strain rate and differential stress in the quasi-viscous material for different strain rates and microscopic viscosity parameters  $A$ . The symbols show measured data, the lines show a linear least squares fit to the data points. The small inset graph shows the relation between the microscopic viscosity parameter and the macroscopic viscosity estimated from the linear fit to the respective stress-strain data.

involved, i.e.  $d_{ab} = \pi((r_a + r_b)/2)^2$  in 3D or  $d_{ab} = (r_a + r_b)/2$  in 2D, respectively. The relative velocity of the particles  $\Delta v_{ab} = v_a - v_b$  is calculated from the difference of the particle velocities  $v_a$  and  $v_b$ . The factor “ $A$ ” is a material constant which can be considered as a microscopic viscosity parameter. Compared with the standard frictional forces usually implemented in DEM [Place and Mora, 1999]:

$$f_{ab}^{fric} = -\mu F_{ab}^n \frac{v_{ab}}{|v_{ab}|} \quad (4)$$

where  $F_{ab}^n$  is the normal force and the relative velocity between the particles is only used to determine the direction of the force the “dashpot” interaction replaces the stress dependent dissipation term with a velocity dependent dissipation.

#### 4. Material Calibration

[14] In DEM there is no analytical relationship between microscopic parameters and the resulting and macroscopic material properties. In particular, this relationship is influenced by the geometric details of the particle packing. Therefore a calibration is needed to relate the micro- and macro-parameters of a particular DEM material [Potyondy and Cundall, 2004; Schöpfer *et al.*, 2009].

[15] The rheology of the less competent material has been measured using confined compression tests (sections 4.1 and 4.2), in case of the quasi-viscous material for a range of different strain rates. To generate the test specimen for the calibration simulations a square box is filled with a densely packed, stress free, random arrangement of 12.000–13.000 particles with a prescribed size range using the insertion based algorithm of Place and Mora [2001]. For the calibration tests particles with radii between 0.2 and 1.0 model

units are used. The specimen is then confined between 4 servo-controlled plates. A prescribed normal stress is applied to the left and right plate such that after a ramp-up from initially stress free conditions the chosen confining stress is reached. The top and bottom plates are moved towards each other to obtain a prescribed strain rate of the deforming specimen, again including a ramp-up phase during which the final plate velocity is reached.

##### 4.1. Quasi-Viscous Material

[16] The forces which are applied at the model boundaries to obtain the chosen strain rate are measured and the average differential stress in the model is calculated from these. The resulting relation between stress and strain rate is shown in Figure 1. A linear fit to the stress - strain rate data, i.e.  $\Delta\sigma = a\dot{\epsilon} + b$ , at the microscopic viscosity parameters  $A$  used for in the calibration experiments (see Table 1) shows that the material is not perfectly linear viscous but represents a reasonable approximation of a viscous material. In particular one would expect the fitted parameter  $b$  in the above equation to be zero if the material was perfectly viscous but as the calculated values for  $a$  and  $b$  in Table 1 show it is not. There is no analytical relationship between the microscopic viscosity parameter  $A$  and the macroscopic viscosity  $a$  obtained from the linear fit. As expected, the macroscopic viscosity  $a$  increases for increasing  $A$  (see small inset plot in Figure 1). However, the details of the relationship are also dependent on particle size range and distribution. A calibration is therefore necessary for each individual combination of microscopic viscosity and particle packing.

##### 4.2. Frictional Material

[17] For the frictional material the same confined compression setup is used to determine the rheological parameters as for the quasi-viscous material. We have performed confined compression tests for a range of confining stresses and strain rates (3 values each, see Figure 2) while the particle scale material parameter have been kept constant. We have used a low value of  $\mu = 0.1$  for the particle scale friction in order to obtain a low macroscopic friction angle of the model material, enabling stress conditions in the layered models which are conducive to the development of boudin structures.

[18] The friction angle was calculated from the stresses observed on boundary plates of the model by

$$\varphi = \arcsin\left(\frac{\Delta\sigma}{2\bar{\sigma}}\right) = \arcsin\left(\frac{\sigma_1 - \sigma_3}{\sigma_1 + \sigma_3}\right) \quad (5)$$

where  $\sigma_1$  is maximum principal stress, measured on the driving plates and  $\sigma_3$  is the minimum principle stress, which is the applied confining stress in this model.  $\Delta\sigma$  is the

**Table 1.** Rheological Parameters for the Quasi-Viscous Material Calculated From the Calibration Tests<sup>a</sup>

$A$	$a$	$b$
0.03	$2.30 \pm 0.24$	$3.0 \times 10^{-4} \pm 2 \times 10^{-5}$
0.1	$4.03 \pm 0.31$	$3.6 \times 10^{-4} \pm 3 \times 10^{-5}$
0.3	$7.06 \pm 0.51$	$4.5 \times 10^{-4} \pm 5 \times 10^{-5}$

<sup>a</sup>The parameter  $A$  in the first column is the particle scale viscosity constant used in the model (see equation (3)) whereas “ $a$ ” and “ $b$ ” are the fitted macroscopic parameters.

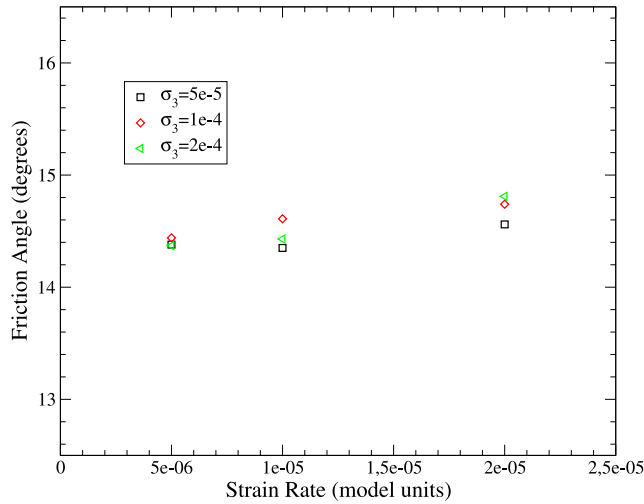


**Figure 2.** Friction angles of the frictional material calculated from calibration tests for a range of strain rates and confining stresses.

differential stress, i.e.  $\sigma_1 - \sigma_3$  and  $\bar{\sigma}$  is the mean stress, i.e.  $(\sigma_1 + \sigma_3)/2$ . The results (Figure 2) show that the model material has a friction angle of  $\varphi = 14.52 \pm 0.16^\circ$  which does not depend significantly on the strain rate.

#### 4.3. Brittle to Semi-Ductile Material (Competent Layer)

[19] For the competent layer a cohesive material was used in which the particles are initially connected by breakable elastic bonds [Wang *et al.*, 2006], using the “Brittle Beam” parametrization of the particle-scale parameters implemented in ESyS-Particle [Weatherley, 2011]. The fracture behavior of this material was varied between fully brittle and semi-ductile by removing a defined fraction of the bonds similar to Schöpfer *et al.* [2009]. The compressive and tensile strength of the material have been calibrated using biaxial compression and confined direct tension tests. By performing a range of simulations with different values of confining stress we obtain approximate failure envelopes for two material configurations, one fully bonded, the other one with 50% of the bonds removed. In order to estimate the influence of the random particle packing on the measured macroscopic properties, 3 random realizations of each material setup were used (see Figure 3). The Mohr-Coulomb failure stresses have been calculated using the closed-form equations to obtain piecewise linear failure envelopes as described by Pincus [2000] the resulting on-circle midpoints are plotted in Figure 3. A nearly linear shape of the failure envelope in the compressive field is observed for both materials whereas the failure envelope becomes highly nonlinear towards the tensile field. This observation is similar to the data obtained from 3D models by Schöpfer *et al.* [2009]. The calculated friction angles are  $\varphi = 24.3 \pm 0.8^\circ$  for the fully bonded case and  $\varphi = 32.1 \pm 0.5^\circ$  for the material with 50% of the bonds removed, i.e. there is a significant change in friction angle between the two materials. A similar increase in friction angle for a partially bonded material has also been observed in a detailed study of the fracture properties of 3D DEM materials by Schöpfer *et al.* [2009]. As expected, strong differences are also observed in the cohesion and tensile strength values and in the ratio

between unconfined compressive and tensile strength (UCS/TS) which is  $\approx 2.9$  in the fully bonded material and  $\approx 10$ –11 in the material with 50% of the bonds removed. The nonlinear shape of the failure envelope in the tensile field for the fully bonded material is consistent with what has been observed in DEM simulations of similar materials in 3D [Schöpfer *et al.*, 2009]. However, a difference between the fully bonded 2D material and its 3D equivalent, i.e. using the same particle size range  $r = 0.2 \dots 1.0$ , is that the 3D material does not show such an extremely low UCS/TS ratio. To verify that a change of the particle scale cohesion does lead to a corresponding proportional change in the macroscopic material strength we performed a series of unconfined compression and tension tests using different particle scale cohesion but identical model geometry and particle packing. The results show a near perfect linear dependence of the unconfined compressive and tensile strength of the model material on the particle scale cohesion. The correlation coefficient is  $r^2 \gg 0.99$  in both cases.

#### 5. Model

[20] Our models contain processes operating on two widely different time scales. The time scale of the fast process, i.e. the dynamic crack propagation across the competent layer, is, depending on the thickness of the layer, in the sub-second to millisecond range. The large scale deformation of the multi-layer package however, can be assumed to take thousands to millions of years, i.e.  $10^{10} \dots 10^{13}$  seconds [Schenk *et al.*, 2007]. Current modeling approaches are unable to accommodate two such different time scale. The main reason is that the size of the time step in the model is determined by the time scale of the fast processes, specifically by the propagation speed of elastic deformations and the size of the particles [Cundall and Strack, 1979; Mora and Place, 1994]. This results in a total number of time steps proportional to the ratio of the time scales. Therefore measures have to be taken to reduce the gap between the time scales in the model in order to make it computationally feasible while still keeping the two scales far enough apart to avoid influencing the model dynamics. An approach often used in discrete element models to achieve this is the so-called “density scaling” [Thornton, 2000]. There the particle

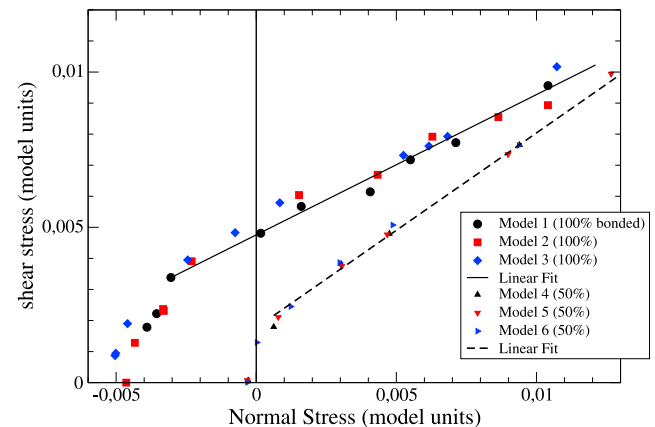


**Figure 3.** Mohr-Coulomb failure stresses for the brittle material (fully bonded and 50% bonded) and linear fit failure envelope for the compressive regime.



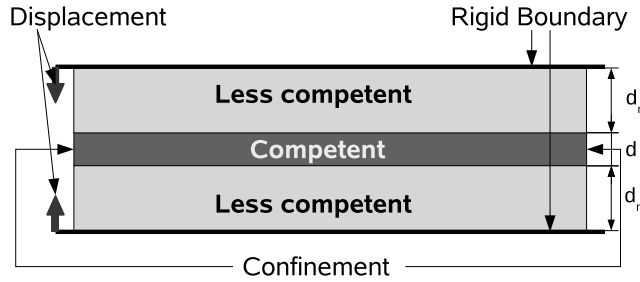


**Figure 4.** Schematic drawing of the model setup.

inertia used in the calculation of particle motion from Newton's law is increased by several orders of magnitude. Because the elastic wave speed in a DEM model is inversely proportional to the square root of inertia of the particles this has the effect of slowing down elastic wave propagation and processes connected with it, such as dynamic crack propagation. Importantly, it also allows the use of larger time steps. To make sure that the dynamic time scale and the long term deformation time scale are still well separated in the model, i.e. the models can still be considered quasi-static, we made sure that the total kinetic energy in the models is small compared to the total energy. Keeping the kinetic energy in the model sufficiently small also ensures that erroneous inertial effects due to the reduced separation of the time scales are negligible.

### 5.1. Model Setup

[21] We use a simple 3 layer model, consisting of a competent layer embedded between two less competent “matrix” layers (Figure 4). The thickness  $d_n$  of the outer (matrix) layers was chosen twice as large as the thickness  $d$  of the central layer. Both matrix layers have the same thickness, i.e. the model is symmetric. The thickness ratio  $d_n/d = 2.0$  has been chosen because it results in a relatively small model size while still avoiding boundary effects from influencing the model dynamics. It would be desirable to minimize the thickness of the outer layer in order to reduce the computational cost of the model, however, models of fracture saturation in multilayer assemblies [Bai and Pollard, 1999] have shown that the critical length to thickness ratio of the boudin blocks can depend on the thickness of the matrix layers if the layer thickness ratio is too small, i.e.  $d_n/d < 1.5$ .

[22] The model boundaries consist of 4 rigid boundary plates. The layer-parallel boundary plates are used to apply a confining stress while the boundary plates perpendicular to the layer are used to apply a extensional strain in the layer-parallel (x) direction on the model. For this purpose these plates are moved apart at a constant velocity, except for the initial phase of the movement where the velocity is ramped up linearly until the chosen speed is reached. In the models using the quasi-viscous material (section 3) the strain rate can be adjusted to obtain the desired level of flow stress in the matrix layers. In the models using the frictional material (section 4.2) the stress state is largely independent of the deformation speed as long as the plate movement is slow enough so that the deformation remains quasi-static. The layer-perpendicular plates are used to apply a constant confining stress to the model.

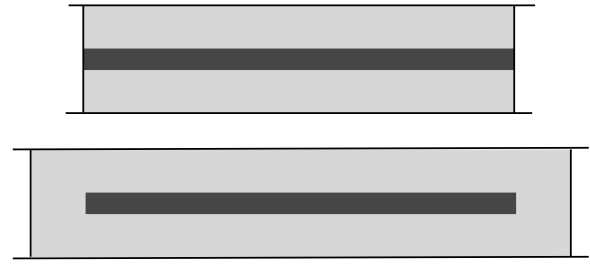


**Figure 5.** Model configurations with different layer ends: (top) open and welded and (bottom) finite.

[23] The models used for the main calculations have an overall aspect ratio of 4:1 while the initial aspect ratio of the competent layer is 20:1. These models consist of approximately 200,000 particles with radii between 0.2 and 1.0 model units. Computing time on 8 CPU cores of the HPC cluster at RWTH Aachen University (Intel Xeon X5570, 2.93 GHz) ranges from 4 h to about 24 h, depending on the final strain and the strain rate. Calibration and test simulations have been performed using smaller models with 12,000 to 50,000 particles.

### 5.2. The Ends of the Layer

[24] The theoretical boudin models [Ramberg, 1955; Mandl, 2005; Li and Yang, 2007; Iyer and Podladchikov, 2009] all implicitly assume that the layered sequence of rocks is infinite in the layer-parallel direction. This can not be implemented directly in a numerical model. We therefore used a model with a finite length. In order to evaluate the influence of the different finite model size we tested 3 different shapes of the layer ends: “open,” i.e. the competent layer extends over the full length of the model but is not connected to the side plates (Figure 5, top), “welded,” using the same model geometry as the open shape but the competent layer is welded to the side plates (Figure 5, top), and “finite,” where the competent layer is slightly shorter than

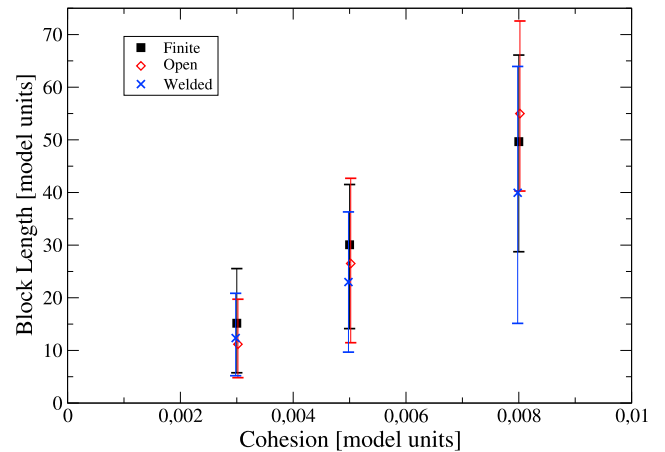


**Figure 6.** Mean block length for models with different layer end conditions as described in section 5.2 at a range of cohesion values of the competent layer. Error bars show the 10th and 90th percentile of the block length distribution, averaged over 3 realizations of each model.

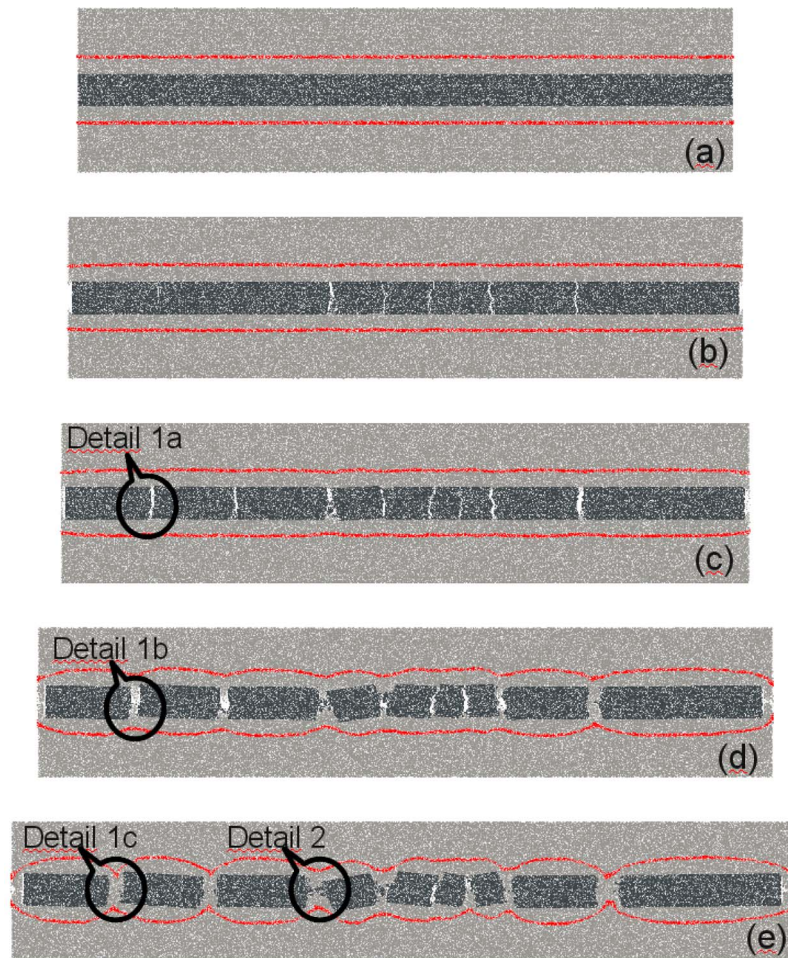


**Figure 7.** Evolution of boudinage in a model using a quasi-viscous matrix material. Light gray, matrix material; dark gray, competent layer (brittle). The red layers are passive markers showing the material flow within the matrix. The snapshots show the model (a) in the initial configuration, (b) after 3% horizontal extension, (c) 5% extension, (d) 12% extension, and (e) 20% extension.

the whole model and therefore the side plates interact only with the matrix material (see Figure 5, bottom).

[25] For identical material properties and boundary conditions we observe that the mean block size and the range of block sizes are very similar between the models with different layer ends (Figure 6). In particular we observe that the scatter within each class of models is larger than the difference between the model classes. For further investigations we therefore chose the model which is computationally cheapest, i.e. the model (a) with straight layer ends which are not welded to the boundary plate.

## 6. Results

### 6.1. General Structures

[26] During the initial phase of the brittle failure of the competent layer tensile cracks form (Detail 1a in Figure 7). Most of these cracks are present very early in the deformation, after less than 1% extension of the competent layer. With increasing extension of the layer these tensile cracks evolve into open cavities (Detail 1b in Figure 7) before getting filled by the inflow of matrix material (Detail 1c in Figure 7).

[27] In some cases the flow of matrix material into an opening crack between two boudin blocks leads to some loose material, either generated in the fracture process or abraded from the block faces by the matrix material moving in, pushed towards the center of the crack. This results in a narrow sliver of material from the competent layer located roughly in the center of the space between the boudin blocks and compressed horizontally by the matrix material flowing into this space from both sides (Detail 2 in Figure 7). Very similar structures have been observed in boudinaged amphibolite layers from Naxos (Figure 8). The deformation of passive marker lines in the matrix which are initially parallel to the competent layer (Figures 7, 9, and 10) shows a smooth deformation pattern in the matrix. Similar displacement patterns have been observed in field examples. Figure 11 shows a boudinaged amphibolite layer in a marble matrix from Naxos, Greece. We assume that the narrow amphibolite layer below the main boudin train is sufficiently thin so that it is mechanically unimportant and can therefore be considered a passive indicator of matrix flow. Comparing the shape of this layer with the deformed marker lines in our models suggests that the patterns of the matrix flow is not



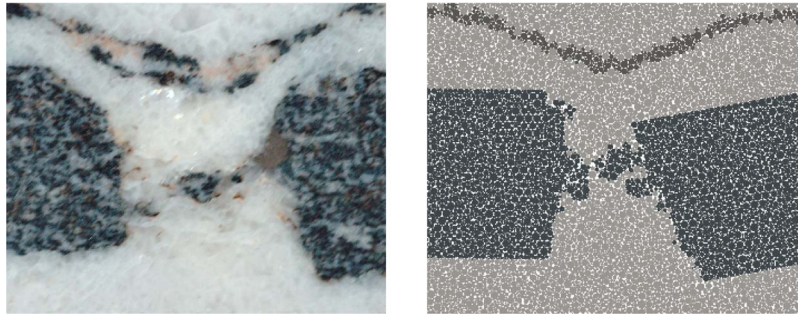


**Figure 8.** (left) Detail of a boudinaged amphibolite layer in marble, and (right) a very similar structure from the numerical model BD057 (viscous matrix).

significantly different between the models and the natural example.

[28] Comparing two models with similar bulk strength in the competent layer but Mohr-Coulomb matrix material in one case (Figure 9) and a quasi-viscous matrix material in the other case (Figure 7) we see that the shapes of the boudins are not significantly different. There is the suggestion of a small

difference in curvature of the deformed marker lines between the two models, indicating that the flow patterns in the matrix are slightly different, but a quantitative investigation of the possible differences is beyond the scope of this work.

[29] The type of boudin which develops in our models is dependent on the material properties of the competent layer. Figure 10 shows the structures which result from a variation

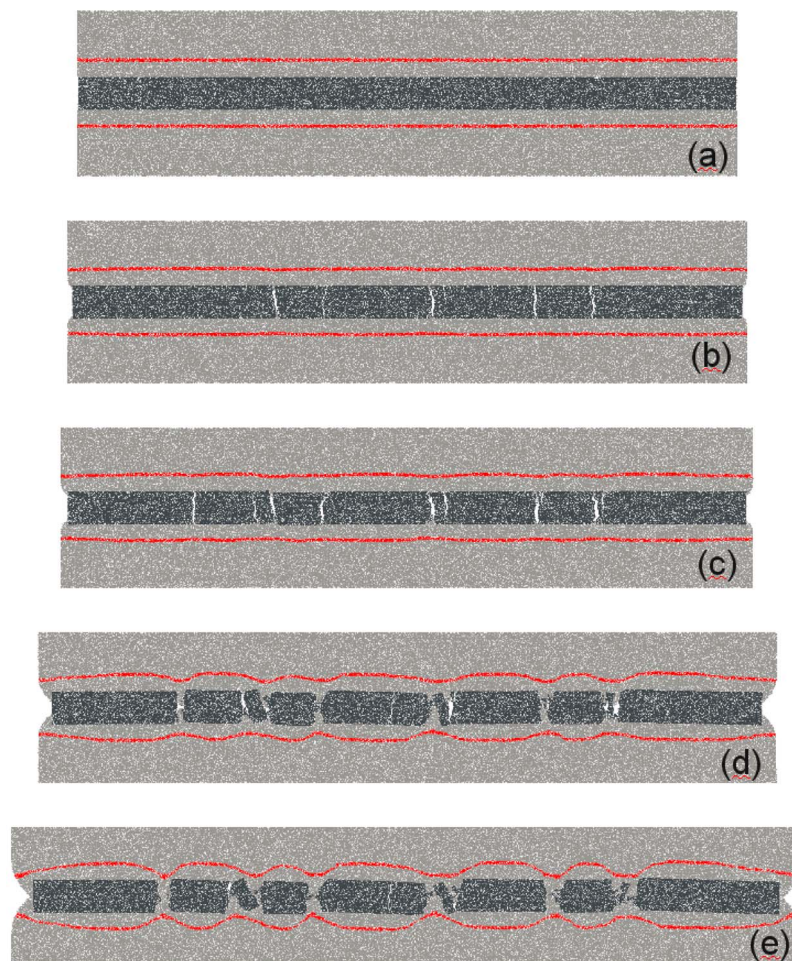


**Figure 9.** Evolution of boudinage in a model using a Mohr-coulomb frictional matrix material. Light gray, matrix material; dark gray, competent layer (brittle). The red layers are passive markers showing the material flow within the matrix. The snapshots show the model (a) in the initial configuration, (b) after 3% horizontal extension, (c) 5% extension, (d) 12% extension, and (e) 20% extension.



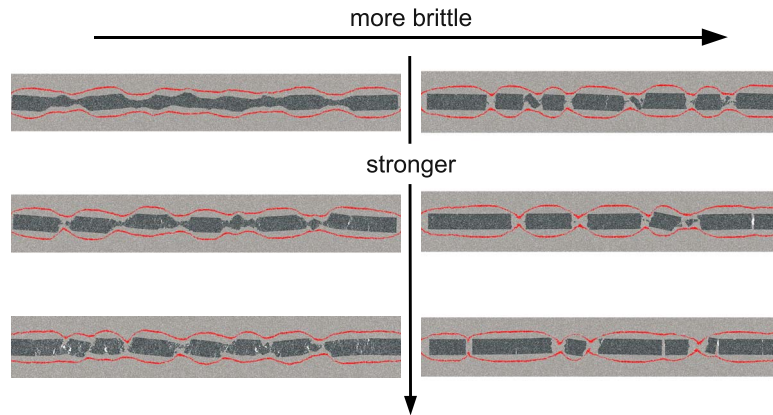


**Figure 10.** Final state of models with different strength and brittleness of the competent layer. All models are using the same Mohr-Coulomb matrix material.

of the strength and the ductility of the competent layer while keeping the matrix rheology constant. We observe that for a fully brittle material we obtain torn boudins with nearly straight faces and the variation in strength mainly influences the fragment size. Using a semi-ductile material where only 50% of the particle bonds are initially present we see a transition from torn boudins at high material strength to pinch and swell structure at low strength.

[30] Using the boudin classification by *Goscombe et al.* [2004] we observe a number of the boudin types described there. In our models pinch-and-swell structures develop in the models with the least competence contrast between the layers, i.e. the weakest central layer material. Asymmetric, shear band boudins develop in the models with intermediate competence contrast while nearly straight sided torn boudins are observed in the models with the strongest central layer. The boudin faces in our models are not absolutely straight but because the faces show undulating rather than simple convex or concave shapes it is not possible to calculate the face curvature (i.e. the  $B_f$  value of *Goscombe et al.* [2004]). However, we do observe that the layer-parallel sides of the fragment remain straight in our models, i.e. the exterior curvature ( $B_b$ ) is zero except in the case of pinch and swell structures. A further interesting observation is that increasing bulk deformation can lead to a change in boudin geometry resulting in a different classification according to *Goscombe et al.* [2004, Figure 3]. Looking at the evolution

of the boudin geometry in Figure 7 we observe that in the central part of the model a transition from “blocky boudins” at the intermediate stages (Figures 7c and 7d) towards “Dilatational Domino Boudins” at the final stage (Figure 7e) takes place.

## 6.2. Fracturing

[31] We have calculated the traction forces exerted on the competent layer by the matrix by adding up the layer-parallel component of the particle interaction forces across the matrix-layer interface. Plotting the traction force along the layer (Figure 12) shows that the force distribution is approximately triangular over length of the still intact layer before the break and after the break it reconfigures into two roughly triangular distributions on the two fragments. Comparing the breaking forces calculated from the interface traction with those expected from the calibration of the material strength we observe that the actual breaking forces are higher than expected. The reason for this observation lies in the heterogeneity of the material strength, i.e. in the compression and tension tests performed in section 4, where the model is loaded from the ends we have a homogeneous stress distribution and therefore the material will always break at its weakest location. In the boudinage models however, the stress distribution is not homogeneous and the competent layer will only break in its weakest spot if this coincides with the location of the peak stress.

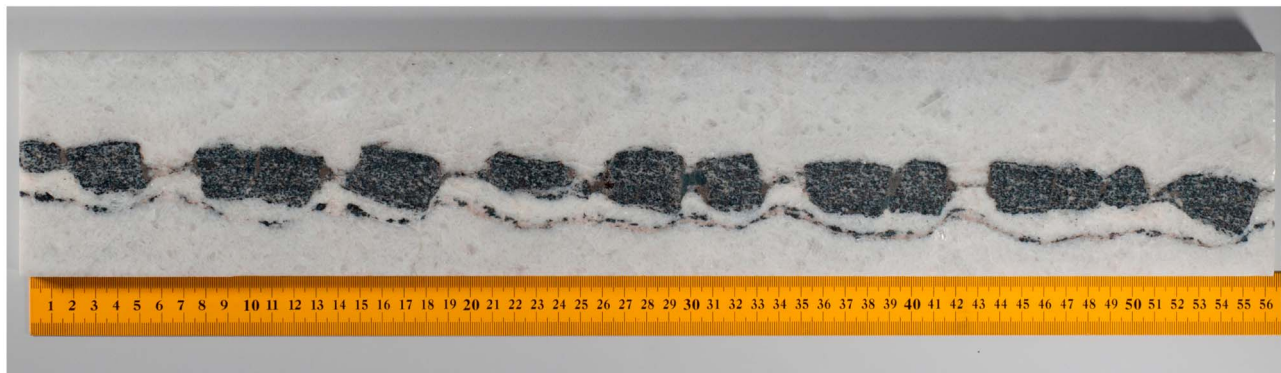


**Figure 11.** Boudinaged amphibolite layer in marble matrix from Naxos, Greece.

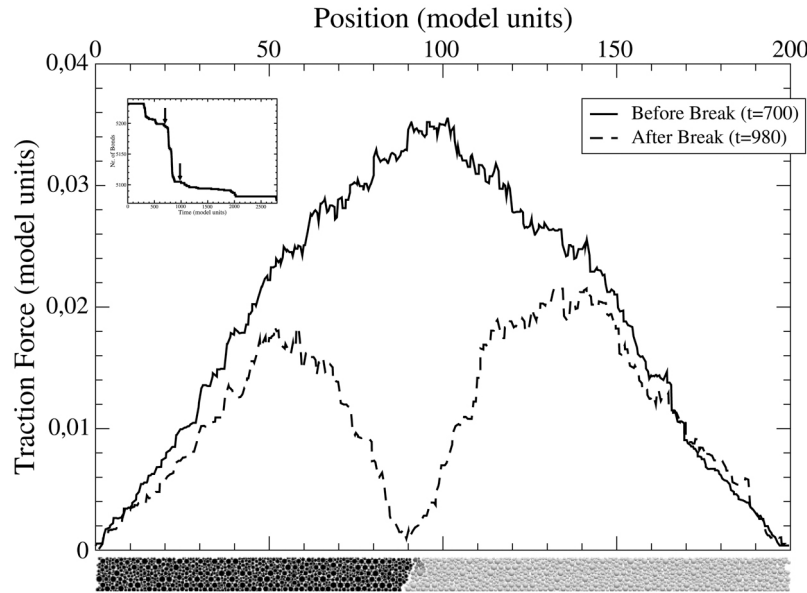


**Figure 12.** Traction forces exerted on the competent layer before and after fracturing. The image below the plot shows the configuration of the fractured competent layer after breaking. Particles are colored by displacement, dark to the left ( $-x$ ) and light to the right ( $+x$ ). The small inset shows the evolution of the number of bonds in the model with the arrows indicating the timing of the pre- and post-fracture data displayed in the main plot.

[32] As predicted by the theoretical models we observe that a variation in the tensile strength of the competent material (see section 4) results in a corresponding variation of the boudin block length (Figures 13 and 10, right column). We are, however, not able to distinguish between the different relations between material strength to block length depending on the exact rheology of the matrix material (equations (1) and (2)). The reasons are the relative large scatter of the block lengths due to the heterogeneous material strength and the fact that the rheology of the quasi-viscous matrix material is not perfectly linear viscous.

[33] The length to thickness ratio of boudin blocks observed in the models covers wide range between 7:1 and 1:1. In addition some very small blocks occur at the end of larger blocks in some cases. These small blocks, which only occur in case that the competent layer consists of the fully brittle material, are produced by small fragments breaking off faces of long boudin blocks due to corner flow effects. After one crack is established (Figure 14a) and the boudin blocks have started to separate, the matrix material is starting to flow into the crack, causing bending stresses on the corners of the blocks, in particular if these corners have a sharp angle due to a concave shape of the block face. These bending stresses can in some cases lead to the initiation of cracks near the block corners, usually starting at the interface between competent layer and matrix (Figure 14b) which can grow towards the center of the competent layer due to the continuing bending stresses. If two cracks originating from different sides of the competent layer coalesce (Figures 14c and 14d), a new, very narrow boudin block is created.

### 6.3. Block Rotations

[34] In some of the models we observe rotations of the bouding blocks (Figure 15) despite the fact that the principal

stress orientations are aligned with the layer orientation and the strains are such that the model does not experience bulk shear. These models generally fall into the category of “extensional shear fracture boudinage” or “Type 2b” of *Mandal et al.* [2000]. The sense of rotation is clearly correlated with the shape of the blocks, i.e. rhombic blocks with a positive angle  $\Phi$  between block end surface and layer normal direction rotate clockwise, those with negative  $\Phi$  rotate anticlockwise and trapezoidal blocks with a different sign of

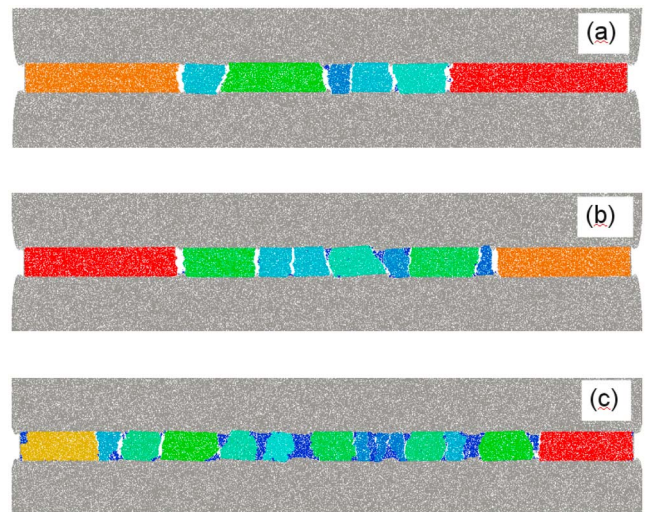


**Figure 13.** Boudin blocks after 10% horizontal extension for models with tensile strength of (a) 0.005, (b) 0.003, and (c) 0.002. Blocks are colored by size, matrix material is gray.



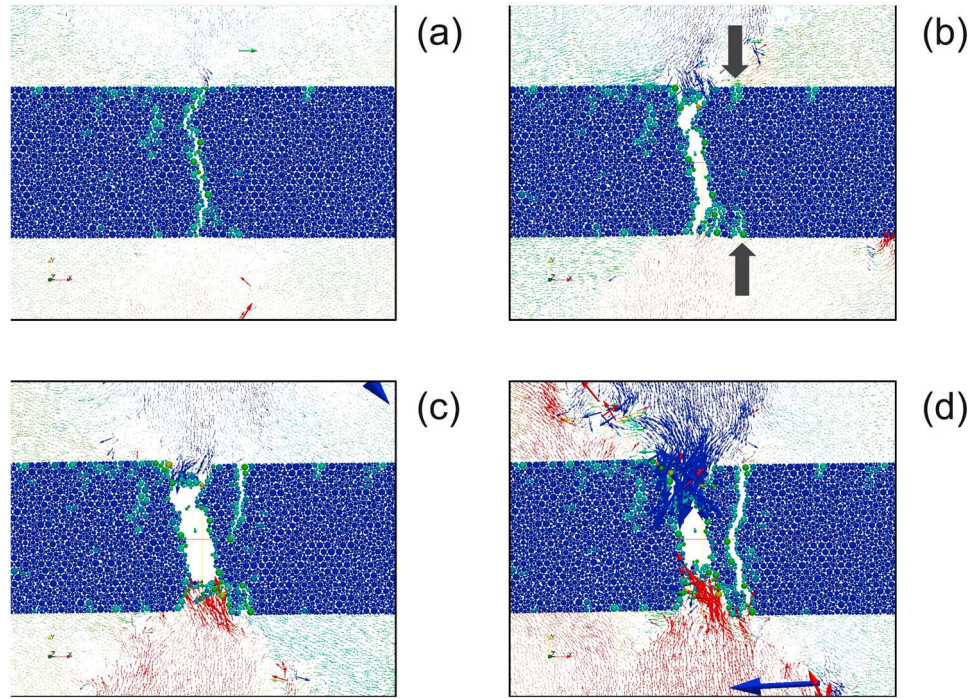


**Figure 14.** (a–d) Sequence of fracturing events leading to the generation of a very small boudin block.

$\Phi$  for both ends do not significantly rotate. The shape of rhombic blocks can be parameterized by the aspect ratio and the angle of the block ends relative to the layer. The length to layer thickness ratio measured in our model is  $L/d \approx 1.47 \dots 2.85$ . Therefore the parameter  $G_r$  used by Mandal and Khan [Mandal and Khan, 1991], which is the width to length ratio would be  $G_r \approx 0.35 \dots 0.68$ . The absolute value of the angle  $\Phi$  between block end surface and layer normal direction is in the range  $\Phi \approx 18 \dots 32^\circ$ . These parameters are similar to experiments “a” ( $G_r = 0.5$ ,  $\Phi = 30^\circ$ ) and “c” ( $G_r = 1.0$ ,  $\Phi = 26^\circ$ ) of Mandal and Khan [1991]. Our model would therefore plot below the solid line in Diagram 7 of Mandal and Khan [1991], i.e. it is expected to produce separation between the blocks. This is consistent with the observed configuration.

[35] The shape and rotation of the boudin blocks in this model is similar to boudins observed in pegmatites in Naxos

[Schenk *et al.*, 2007], which are also believed to have formed without bulk layer parallel shear. However, unlike the two-phase model including the reactivation of mode-I fractures under decreasing pore pressure proposed there, the block rotations in our model occur in a single deformation phase. In the model shown here the initial failure of the brittle layer happens in shear, not in tensile mode as proposed for the pegmatites in Naxos, due to the different stress regimes and in particular the absence of pore fluid and the related reduction in effective mean stress in our model.

[36] We also see an increase of block rotations if the confining stress is increased (Figure 16). This can be partially explained by the transition from tensile to hybrid or shear failure leading to failure planes orientated obliquely to the layering and therefore the generation of asymmetric boudin blocks. The increase in mean stress also makes it more difficult to form open cavities between the blocks,

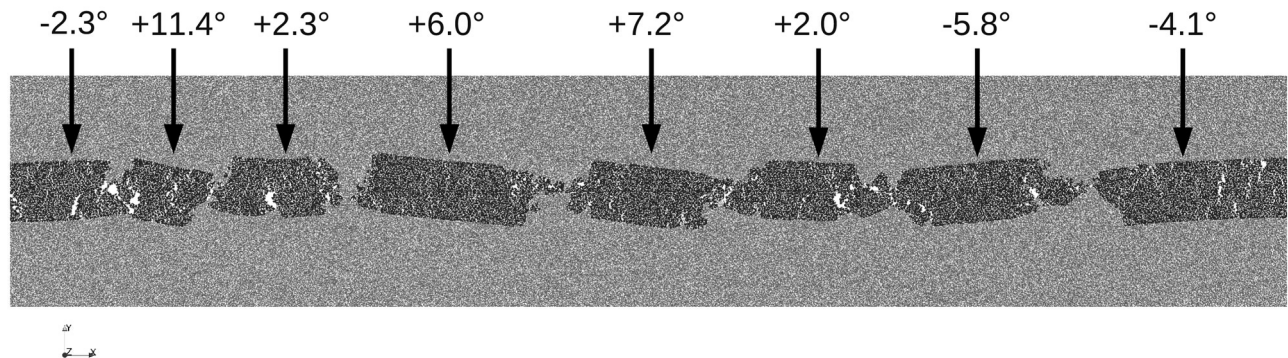


**Figure 15.** Final configuration of boudinaged layer in Model B007 with the amount of rotation indicated for each block. Positive rotation angles are clockwise, negative values are counterclockwise.

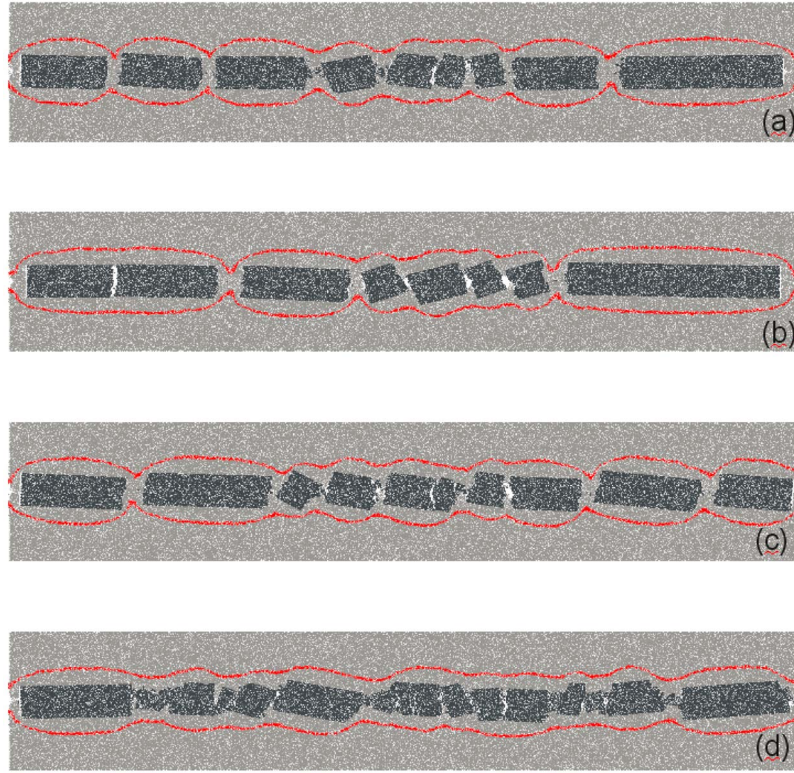


**Figure 16.** Final configurations in Models with different confining stress. Confinement is increasing from Figure 16a to Figure 16d.

leading to a flexural cantilever effect enhancing block rotations.

## 7. Discussion

[37] We have used two different types of ductile material in our DEM models of boudinage, one frictional and one quasi-viscous. We have shown that using “dashpot” interactions between particles results in a reasonable first order approximation of viscous behavior, although the relation between stress and strain rate is not exactly linear. Under the deformation conditions applied in our models the rheology we obtain is closer to a Bingham material [Middleton and Wilcock, 1994; Twiss and Moores, 2007]. While this does not represent an exact quantitative match of the natural materials we intend to simulate in our models, results have shown that we can obtain realistic first order structures despite the simplified material behavior. Additionally, it has been shown that the rheology of silicone putty, a material which is often used in analogue models, can be approximated as a Bingham material [Dixon and Summers, 1986].

[38] Our results (Figures 7 and 9) show that the structures in the boudinaged layer are not significantly influenced by details of rheology of the surrounding material, at least for the types of material used in our models. A different behavior might result if a matrix material is used which supports the localization of the deformation. This would require strain- or strain-rate dependent weakening of the material strength, which both model materials used here do not show. Data obtained from a parameter space study over a range of material properties suggests that the strongest factor

influencing the structures is the failure and post-failure behavior of competent layer itself.

[39] The observation that boudin block rotation, even in the case of purely coaxial deformation (despite no layer-parallel shear), is interesting because block rotation is often seen as an indicator to determine bulk shear sense [Hanmer, 1986; Goldstein, 1988; Goscombe and Passchier, 2003]. Rotations of boudin blocks has been demonstrated before by Passchier and Druguet [2002] using a pre-broken competent layer. The results obtained in this work for the case of a boudin train oriented initially parallel to the bulk extension direction and no vorticity in the bulk flow field (i.e. the  $\Psi = 0$ ,  $W_k = 0$  case of Passchier and Druguet [2002]) are consistent with our model. A key difference, however, is that in our model the all block end faces are oriented in the same direction but that the both possible conjugate orientations of the shear failure plane are present. Therefore we see rhombic blocks with positive and negative angles between the layer normal and the end face and also trapezoidal blocks in cases where the two end faces of a block are oriented differently. Consequently we also observe different rotation directions for different block shapes. This could provide an indication to distinguish between block rotation due to bulk vorticity and block rotation due to block shape effects in coaxial deformation.

[40] In rocks where fluids are present the formation of open cracks between boudin blocks which has been observed in our models would result in the incursion of the fluids into these cavities and potentially to the precipitation of dissolved materials and the formation of a vein. The relative speed of fluid incursion, vein formation and the inflow



of matrix material will be determined by, amongst other parameters, the pore fluid pressure, the permeability of matrix and competent layer material, the viscosity of the matrix material and the opening rate of the crack. While the modeling of those processes is beyond the scope of the current model we need to acknowledge that our model probably underestimates the speed with which the matrix material flows into the opening cracks, in particular in the early phase when the crack is narrow. The reason is the finite spatial resolution of the model which is determined by the particle size. If the crack is narrower than the diameter of the matrix particle located at the crack opening no material will move into the crack but even if the crack is slightly wider there is still the possibility of grain bridging obstructing the flow of material into the crack. Only after the crack has widened sufficiently the matrix material can flow in a natural way.

[41] The model is still limited by not including a number of processes which are potentially important for the evolution of boudinage structures. We therefore do not observe the full spectrum of boudin shapes seen in natural examples [cf. Goscombe *et al.*, 2004]. In particular we do not observe certain types of boudins which show strongly concave end faces (i.e. “Fishmouth boudins”) or have a curved exterior. There is a range of possible explanations why we don’t generate these boudin types in our model related to the simplifications employed. One potentially important aspect is that the current material properties of the competent layer do not allow pre-fracture ductile deformation. Also, the model does not contain a mechanism to allow vein formation in the boudin necks which might influence the shape of the end faces of the boudin blocks. Observations [Weiss, 1972] of veins between concave boudin blocks suggests that there is a connection. We also have to consider that some of the boudin shapes observed in nature are the result of multi-stage deformation processes such as the ones described by Schenk *et al.* [2007] or that the shapes are evolving by ductile deformation post-fracture [Maeder *et al.*, 2009].

## 8. Conclusions

[42] We have shown that the DEM approach is suitable to model many aspects of the full boudinage process from the initial fracturing to the separation of the blocks and the filling of the gaps with matrix material. Our results demonstrate that a key factor responsible for the wide range of boudin shapes observed is the material behavior of the competent layer whereas the rheology of the matrix material appears to be of secondary importance. We have also shown that the post-fracture movement of the boudin blocks can lead to block rotations and the generation of dilatational domino boudins under purely coaxial bulk deformation, which may be an important aspect when considering rotated boudins as shear sense indicators.

[43] In future work a better approximation of a linear and possibly a non-linear viscous matrix material will be necessary to enable a more quantitative investigation of the influence of the matrix rheology. Also, an important next step will be to make the transition from 2D to a 3D model.

[44] **Acknowledgments.** We thank the Ministry of Oil and Gas of the Sultanate of Oman and Petroleum Development Oman LLC (PDO) for granting permission to publish the results of this study. We also thank PDO for providing support for this work and Gideon Lopez Cardozo for

useful discussion. We thank RWTH Aachen University for enabling the performance of the main computations at the High Performance Computing Cluster at RWTH Aachen University. We also thank Frederic Gueydan and an anonymous reviewer for their helpful reviews.

## References

- Abe, S., D. Place, and P. Mora (2003), A parallel implementation of the lattice solid model for the simulation of rock mechanics and earthquake dynamics, *Pure Appl. Geophys.*, **161**, 2265–2277.
- Abe, S., S. Latham, L. Gross, and J. Smilie (2005), Coupling finite elements and particle based methods, in *International Conference on Computational Methods of Coupled Problems in Science and Engineering COUPLED PROBLEMS 2005*, edited by M. Papadarakakis, E. Oñate, and B. Schreffler, pp. 194, Cent. Int. de Métodos Numér. en Ing., Barcelona, Spain.
- Bai, T., and D. D. Pollard (1999), Spacing of fractures in a multilayer at fracture saturation, *Int. J. Fract.*, **100**, L23–L28.
- Bai, T., D. Pollard, and H. Gao (2000), Explanation for fracture spacing in layered materials, *Nature*, **403**, 753–755.
- Cundall, P. A., and O. Strack (1979), A discrete numerical model for granular assemblies, *Géotechnique*, **29**, 47–65.
- Dixon, J., and J. Summers (1986), Another word on the rheology of silicone putty: Bingham, *J. Struct. Geol.*, **8**(5), 593–595, doi:10.1016/0191-8141(86)90010-6.
- Ghosh, S. (1988), Theory of chocolate tablet boudinage, *J. Struct. Geol.*, **10**(6), 541–553, doi:10.1016/0191-8141(88)90022-3.
- Goldstein, A. G. (1988), Factors affecting the kinematic interpretation of asymmetric boudinage in shear zones, *J. Struct. Geol.*, **10**(7), 707–715.
- Goscombe, B., and C. Passchier (2003), Asymmetric boudins as shear sense indicators: An assessment from field data, *J. Struct. Geol.*, **25**(4), 575–589.
- Goscombe, B. D., C. W. Passchier, and M. Hand (2004), Boudinage classification: End-member boudin types and modified boudin structures, *J. Struct. Geol.*, **26**(4), 739–763.
- Hanmer, S. (1986), Asymmetric pull-aparts and foliation fish as kinematic indicators, *J. Struct. Geol.*, **8**(2), 111–122.
- Harris, L., and H. Koyi (2003), Centrifuge modelling of folding in high-grade rocks during rifting, *J. Struct. Geol.*, **25**(2), 291–305, doi:10.1016/S0191-8141(02)00018-4.
- Iyer, K., and Y. Y. Podladchikov (2009), Transformation-induced jointing as a gouge for interfacial slip and rock strength, *Earth Planet. Sci. Lett.*, **280**, 159–166.
- Kenis, I., J. Urai, W. van der Zee, C. Hilgers, and M. Sintubin (2005), Rheology of fine-grained siliciclastic rocks in the middle crust—evidence from structural and numerical analysis, *Earth Planet. Sci. Lett.*, **233**, 351–360, doi:10.1016/j.epsl.2005.02.007.
- Kidan, T., and J. Cosgrove (1996), The deformation of multilayers by layer-normal an experimental investigation, *J. Struct. Geol.*, **18**(4), 461–474.
- Kobberger, G., and G. Zulauf (1995), Experimental folding and boudinage under pure constrictional conditions, *J. Struct. Geol.*, **17**(7), 1055–1063, doi:10.1016/0191-8141(94)00130-R.
- Kukla, P. A., L. Reuning, S. Becker, J. L. Urai, and J. Schönherr (2011), Distribution and mechanisms of overpressure generation and deflation in the late neoproterozoic to early cambrian south Oman salt basin, *Geofluids*, **11**, 349–361.
- Li, Y., and C. Yang (2007), On fracture saturation in layered rocks, *Int. J. Rock Mech. Min. Sci.*, **44**, 936–941.
- Maeder, X., C. W. Passchier, and D. Koehn (2009), Modelling of segment structures: Boudins, bone-boudins, mullions and related single- and multiphase deformation features, *J. Struct. Geol.*, **31**(8), 817–830.
- Mandal, N., and D. Khan (1991), Rotation, offset and separation of oblique-fracture (rhombic) boudins: Theory and experiments under layer-normal compression, *J. Struct. Geol.*, **13**(3), 349–356.
- Mandal, N., C. Chakraborty, and S. K. Samanta (2000), Boudinage in multi-layered rocks under layer-normal compression: A theoretical analysis, *J. Struct. Geol.*, **22**(3), 373–382.
- Mandl, G. (2005), *Rock Joints The Mechanical Genesis*, Springer, New York.
- Middleton, G. V., and P. R. Wilcock (1994), *Mechanics in the Earth and Environmental Sciences*, Cambridge Univ. Press, New York.
- Mora, P., and D. Place (1994), Simulation of the frictional stick-slip instability, *Pure Appl. Geophys.*, **143**, 61–87.
- Neurath, C., and R. Smith (1982), The effect of material properties on growth rates of folding and boudinage: Experiments with wax models, *J. Struct. Geol.*, **4**(2), 215–229, doi:10.1016/0191-8141(82)90028-1.
- Passchier, C. W., and E. Druguet (2002), Numerical modelling of asymmetric boudinage, *J. Struct. Geol.*, **24**(11), 1789–1803.
- Pincus, H. (2000), Closed-form/least-squares failure envelopes for rock strength, *Int. J. Rock Mech. Min. Sci.*, **37**, 763–785.

- Place, D., and P. Mora (1999), The lattice solid model: Incorporation of intrinsic friction, *J. Int. Comput. Phys.*, 150, 332–372.
- Place, D., and P. Mora (2001), A random lattice solid model for simulation of fault zone dynamics and fracture process, in *Bifurcation and Localisation Theory for Soils and Rocks 99*, edited by H.-B. Mühlhaus, A. Dyskin, and E. Pasternak, pp. 321–333, A. A. Balkema, Rotterdam, Netherlands.
- Potyondy, D., and P. Cundall (2004), A bonded-particle model for rock, *Int. J. Rock Mech. Min. Sci.*, 41, 1329–1364.
- Radjai, F., and V. Richefeu (2009), Contact dynamics as a nonsmooth discrete element method, *Mech. Mater.*, 41(6), 715–728, doi:10.1016/j.mechmat.2009.01.028.
- Ramberg, H. (1955), Natural and experimental boudinage and pinch-and-swell structures, *J. Geol.*, 63, 512–526.
- Ramsay, J. G., and M. I. Huber (1987), *The Techniques of Modern Structural Geology*, Academic, London.
- Reuning, L., J. Schoenherr, A. Heimann, J. Urai, R. Littke, P. Kukla, and Z. Rawahi (2009), Constraints on the diagenesis, stratigraphy and internal dynamics of the surface-piercing salt domes in the Ghaba Salt Basin (Oman): A comparison to the Ara formation in the South Oman Salt Basin, *GeoArabia*, 32(4), 83–120.
- Schenk, O., J. L. Urai, and W. van der Zee (2007), Evolution of boudins under progressively decreasing pore pressure: A case study of pegmatites enclosed in marble deforming at high grade metamorphic conditions, Naxos, Greece, *Am. J. Sci.*, 307, 1009–1033, doi:10.2475/07.2007.03.
- Schönherr, J., L. Reuning, P. Kukla, R. Littke, J. Urai, and Z. Rawahi (2008), Halite cementation and carbonate diagenesis of intra-salt carbonate reservoirs of the late neoproterozoic to early cambrian ara group (south Oman salt basin), *Sedimentology*, 56(2), 567–589.
- Schöpfer, M. P. J., S. Abe, C. Childs, and J. J. Walsh (2009), The impact of porosity and crack density on the elasticity, strength and friction of cohesive granular materials: Insights from DEM modelling, *Int. J. Rock Mech. Min. Sci.*, 46, 250–261.
- Schöpfer, M. P. J., A. Arslan, J. J. Walsh, and C. Childs (2011), Reconciliation of contrasting theories for fracture spacing in layered rocks, *J. Struct. Geol.*, 33(4), 551–565, doi:10.1016/j.jsg.2011.01.008.
- Thornton, C. (2000), Numerical simulations of deviatoric shear deformation of granular media, *Géotechnique*, 50(1), 43–53.
- Treagus, S., and L. Lan (2004), Deformation of square objects and boudins, *J. Struct. Geol.*, 26(8), 1361–1376, doi:10.1016/j.jsg.2003.12.002.
- Twiss, R. J., and E. M. Moores (2007), *Structural Geology*, 2nd ed., W. H. Freeman, San Francisco, Calif.
- van Gent, H., J. L. Urai, and M. de Keijzer (2011), The internal geometry of salt structures: A first look using 3d seismic data from the Zechstein of the Netherlands, *J. Struct. Geol.*, 33(3), 292–311.
- van Noten, K., and M. Sintubin (2010), Linear to non-linear relationship between vein spacing and layer thickness in centimetre- to decimetre-scale siliciclastic multilayers from the high-ardenne slate belt (Belgium, Germany), *J. Struct. Geol.*, 32(3), 377–391, doi:10.1016/j.jsg.2010.01.011.
- Victor, P., and I. Moretti (2006), Polygonal fault systems and channel boudinage: 3D analysis of multidirectional extension in analogue sandbox experiments, *Mar. Pet. Geol.*, 23, 777–789.
- Wang, Y., S. Abe, S. Latham, and P. Mora (2006), Implementation of particle-scale rotation in the 3-D lattice solid model, *Pure Appl. Geophys.*, 163, 1769–1785.
- Weatherley, D. (2011), Investigations on the role of microstructure in brittle failure using discrete element simulations, *Geophys. Res. Abstr.*, 13, EGU2011–9476.
- Weatherley, D., V. Boros, W. Hancock, and S. Abe (2010), Scaling benchmark of esys-particle for elastic wave propagation simulations, paper presented at Sixth International Conference on eScience, Inst. Electr. and Electr. Eng., Brisbane, Australia.
- Weiss, L. E. (1972), *The Minor Structures of Deformed Rocks: A Photographic Atlas*, Springer, New York.
- Zulauf, G., J. Zulauf, O. Bornemann, N. Kihm, M. Peinl, and F. Zanella (2009), Experimental deformation of a single-layer anhydrite in halite matrix under bulk constriction. Part 1: Geometric and kinematic aspects, *J. Struct. Geol.*, 31(4), 460–474, doi:10.1016/j.jsg.2009.01.013.
- Zulauf, G., J. Zulauf, O. Bornemann, F. Brenker, H. Höfer, M. Peinl, and A. Woodland (2010), Experimental deformation of a single-layer anhydrite in halite matrix under bulk constriction. Part 2: Deformation mechanisms and the role of fluids, *J. Struct. Geol.*, 32(3), 264–277, doi:10.1016/j.jsg.2009.12.001.

S. Abe and J. L. Urai, Geologie-Endogene Dynamik, RWTH Aachen University, Lochnerstr. 4-20, D-52056 Aachen, Germany. (s.abe@ged.rwth-aachen.de; j.urai@ged.rwth-aachen.de)